Composite Structures 292 (2022) 115679

Contents lists available at ScienceDirect

Composite Structures

journal homepage: www.elsevier.com/locate/compstruct

Melted and recrystallized holey-graphene-reinforced aluminum composites: Structure, elasticity and strength

Cátia Guarda [a], Bruno Faria [b], Nuno Silvestre [c,*], José N.C. Lopes [a], Nicola M. Pugno [d,e]

[a] CQE, Department of Chemical Engineering, Instituto Superior Técnico, Universidade de Lisboa, Av. Rovisco Pais, 1049-001 Lisboa, Portugal
[b] IPC-Institute for Polymers and Composites, Polymer Engineering Department, University of Minho, Campus de Azurem, 4804-533-Guimarães, Portugal
[c] IDMEC, Department of Mechanical Engineering, Instituto Superior Técnico, Universidade de Lisboa, Av. Rovisco Pais, 1049-001 Lisboa, Portugal
[d] Laboratory for Bioinspired, Bionic, Nano, Meta Materials & Mechanics, Department of Civil, Environmental and Mechanical Engineering, University of Trento, Via Mesiano 77, 38123 Trento, Italy
[e] School of Engineering and Materials Science, Queen Mary University of London, Mile End Road, London E1 4NS, UK

A B S T R A C T

This paper aims to investigate the elasticity, strength and failure of aluminum (Al) nanocomposites with holey-graphene (hG), which were melted and recrystallized. Five nanocomposites (Al-graphene and four Al-hG - two of them doped, with nitrogen and boron) were studied by molecular dynamics simulations. They were melted and subsequently recrystallized at a fixed cooling rate of 0.25 K/ps. The nucleation temperature of nanocomposites was increased by 300–200 K compared to pure aluminum. The Al crystallization in the nanocomposites was about 85 % (97 % for pure Al). The nanocomposites with undoped nanofillers showed an increase in Young's modulus between 15 and 27 % relative to pure Al, while doped nanofillers showed no improvement. The mechanical properties of the nanocomposites depended on the characteristics of the nanofillers, namely (i) the porosity, (ii) the percentage of recrystallization of the Al matrix, and (iii) the interfacial adhesion in the interface Al-nanofillers. The results show that undoped nanofillers have much higher Young's modulus and lower porosity compared to the doped nanofillers (N-hG and B-hG). Finally, the application of the inverse rule of mixtures to extract the Young's modulus of the nanocomposite was successful.

1. Introduction

Aluminum matrix composites (AMCs) are synthesized by incorporating a certain content of reinforcement phases into the Al matrix [1]. As a vital component of AMCs, the reinforcing phase should meet the following conditions: good mechanical and functional properties as well as great chemical stability and affinity with the Al matrix [2]. Graphene, one of the most important carbon-based materials, is an allotrope of carbon which takes a planar form and is composed of sp^2-bonded atoms. It exhibits exceptional ideal electrical, chemical, physical, optical, and mechanical properties. It has high Young's modulus (0.7 – 1.4 TPa [3]) and ultimate tensile strength (119 – 130 GPa [4]). It also has a high theoretical specific surface area (2630 $m^2\ g^{-1}$), thermal conductivity (~5000 $W\ m^{-1}\ K^{-1}$), and a good electrical conductivity [5]. As a result, graphene is widely considered as one of the ideally strongest reinforcing phases in AMCs. Graphene-reinforced AMCs (GRAMCs) are known to present excellent properties, such as high yield and tensile strength [6,7], low density [8,9], high electrical and thermal conductivity [1,9], low thermal expansion coefficient [9], good hardness and wear resistance [1,10]. However, the interfacial bonding strength between graphene and the Al matrix heavily affects the mechanical properties of the composite. Due to the poor wettability of graphene in the Al matrix, interfacial adhesion is weak, resulting in poor performance of these composite materials [2].

Recently, experimental and theoretical works demonstrate that defects in graphene enhance the mechanical properties of graphene/metal composites significantly [11,12,13,14,15].

Holey graphene (hG) is an unique category of defective graphene material which possesses nanopores in its plane. This porous structure enables easy interaction with organic/inorganic species having broad applications in water treatment and desalination, energy storage systems, and environmental protection [16]. hG exhibits distinct properties from its pristine form. Compared to other graphene based porous materials, hG has an increased surface area, reduced nanosheet stacking, enhanced chemical reactivity and a potential hydrophilic nature due to the introduction of functional groups at the pore edges [16]. Graphene-based porous materials have many merits over other porous carbon materials. (1) The high mechanical strength of graphene ensures the stability of porous frameworks and prevents the deformation of the porous structures. (2) The chemical and thermal stabilities of graphene enable it to withstand rigorous environments. (3) The in-plane pores and interlayer spacing are suitable for the rapid diffusion of ions and

* Corresponding author.
E-mail address: nsilvestre@tecnico.ulisboa.pt (N. Silvestre).

https://doi.org/10.1016/j.compstruct.2022.115679
Received 4 April 2022; Accepted 24 April 2022
Available online 1 May 2022

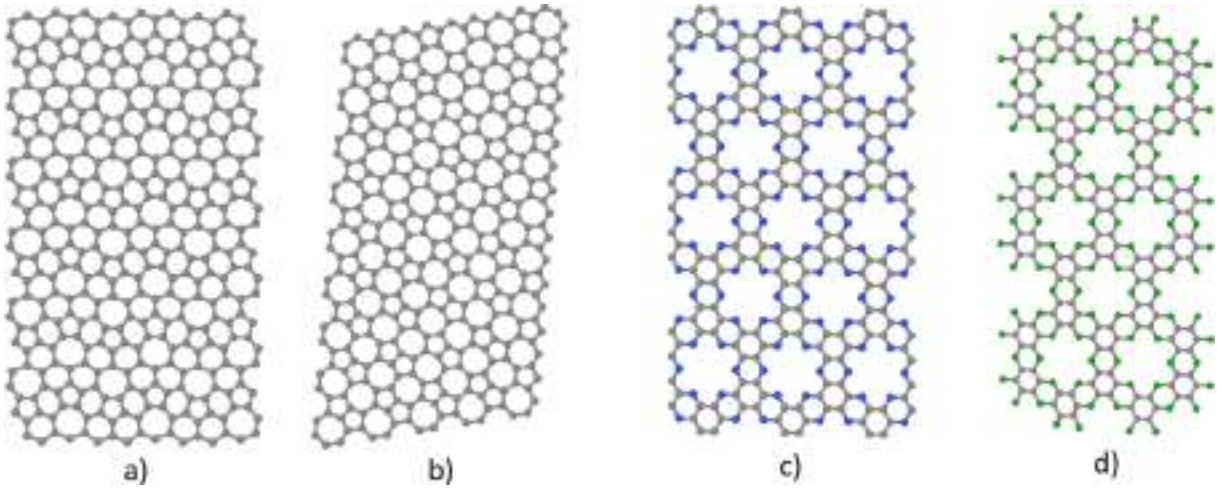

Fig. 1. a) Phagraphene [18], b) R-haeckelite [19], c) N-hG (carbon atoms – grey; N atoms – blue) [20] and d) B-hG (carbon atoms – grey; B atoms – green) [21]. (For interpretation of the references to colour in this figure legend, the reader is referred to the web version of this article.)

Table 1
Structural data on Al matrix and nanocomposites. **a** is the crystal lattice constant; **H** is depth (defined in the [0 1 0] direction of the crystal lattice); **W** is width (defined in the [1 0 0] direction of the crystal lattice); **L** is length (defined in the [0 0 1] direction of the crystal lattice); **N** is the total number of atoms.

Nanocomposite		a (Å)	H (Å)	W (Å)	L (Å)	N
Matrix	Al	4.041	64.8	64.8	81.0	22,325
Sheet	Graphene			19.9	39.4	330
	Phagraphene			21.7	40.5	376
	Haeckelite			22.2	40.4	359
	N-hG			24.1	41.8	318
	B-hG			22.5	46.9	286
Nanocomposite	Al-graphene		64.8	64.8	81.0	22,246
	Al-phagraphene					22,252
	Al-haeckelite					22,235
	Al-N-hG					22,126
	Al-B-hG					22,048

molecules. (4) The narrow pore size distribution range allows accurate control of the pore size for targeted applications. And lastly, (5) the electrical conductivity of graphene makes it an ideal current collector for the fast transportation of charge carriers within the porous structures [17].

The interfacial strengthening mechanism in Al/hG composites has not yet been fully understood from a theoretical perspective. In this work, the way in which the nanopores in hG sheets affect the mechanical properties of Al/hG composites was studied through molecular dynamics simulations. Four well-known hG sheets were used: Phagraphene (PG, Fig. 1a) [18], R-haeckelite (Fig. 1b) [19], nitrogenated hG (N-hG, Fig. 1c) [20] and boronated hG (B-hG, Fig. 1d) [21]. PG, composed of rings containing five, six, and seven carbon atoms, is slightly more unstable than pristine graphene but energetically more stable than other carbon materials. This notable stability comes from carbon bonding with sp^2-hybridization and forming a dense atomic packing structure. PG has direction-dependent Dirac cones [18]. It presents anisotropic and relatively low thermal conductivity: in average of 218 ± 20 Wm^{-1} K^{-1} along the armchair direction and 285 ± 29 Wm^{-1} K^{-1} along the zigzag direction at room temperature [22]. Because of its distinct geometric arrangement of carbon atoms, PG exhibits interesting mechanical properties. A recently theoretical study showed that PG membranes have an elastic modulus of approximately 800 ± 14 GPa [22]. It was also shown that PG membranes might present non-planar configurations, which can significantly influence PG mechanical properties [23].

Haeckelites consist of ordered arrangements of pentagons, hexagons and heptagons with sp^2-bonded carbon atoms [24]. They can be categorized as: (1) Rectangular, containing only heptagons and pentagons paired symmetrically within a flat surface; (2) Hexagonal, which exhibits repetitive units of three agglomerated heptagons, surrounded by alternating pentagons and hexagons; (3) Oblique, containing pentalene and heptalene units bound together and surrounded by six membered rings. Haeckelites are shown to be stable structures, energetically viable, and exhibit an intrinsic metallic behavior independent of orientation [19]. As mentioned earlier, R-haeckelite sheet was used in this work.

N-hG [20] and B-hG [21] are two-dimensional graphene-derived materials with a C_2N or C_2B stoichiometry (C_2N for N-hG or C_2B for B-hG), evenly distributed holes and N or B (N for N-hG or B for B-hG) atoms in its basal plane. N-hG presents a remarkable elastic modulus of 335 ± 5 GPa and tensile strength of 60 GPa (at room temperature), and an intrinsic thermal conductivity of 64.8 W/m-K (at 300 K) [20]. As for B-hG, to the author's knowledge, there are no published reports on its the mechanical properties.

This work employed a molecular dynamics (MD) methodology, which has been previously used by the authors [25]. The nanocomposites were melted and then recrystallized by a cooling procedure. This allowed the Al atoms to organize over the surface of the nanofillers, promoting physisorption and adhesion at the interface. After equilibration, tensile loading was imposed on the solid nanocomposites using two different nanofiller boundary conditions: tensile loading was imposed only to the Al matrix (case A); tensile loading was imposed in both the Al matrix and the nanofiller (case B). Stress–strain and energy-strain curves were obtained. The mechanical properties of the nanocomposites were compared with those of pure Al, which was also melted and recrystallized.

2. Computational approach

2.1. Nanocomposite model

The Al matrix was modelled according to lattice constant in the form of a square prism. The dimensions and number of atoms can be seen in Table 1. Graphene, PG, R-haeckelite, N-hG and B-hG were also modeled. The thickness of nanofillers is the accepted van-der-Waals (vdW) distance for graphene interplanar spacing (3.35 Å).

To obtain the initial configuration of the nanocomposites, a region in the center of the Al matrix with dimensions equal to those of the nanofillers was selected. An additional 2 Å was added to each side to

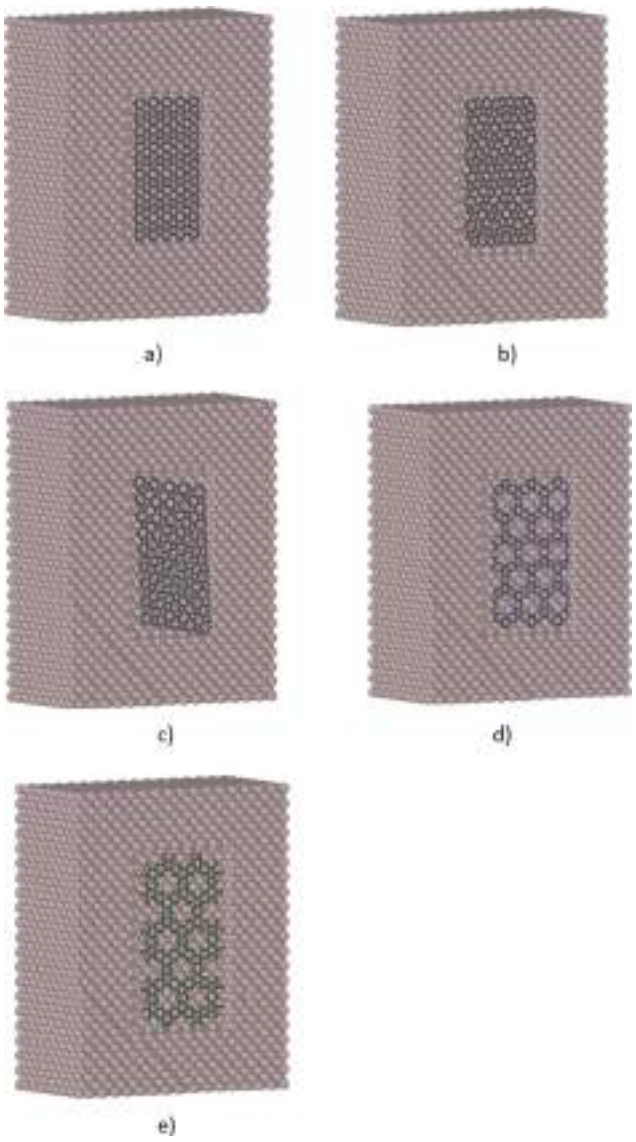

Fig. 2. Representations of a) Al-graphene, b) Al-phagraphene, c) Al-haeckelite, d) Al-N-hG, and **e)** Al-B-hG. The nanocomposites structure was cut in half to show the embedded nanofillers. Al atoms are coloured pink, C atoms are coloured dark gray, N are coloured blue and B are coloured green. (For interpretation of the references to colour in this figure legend, the reader is referred to the web version of this article.)

Table 2
LJ parameters for C-C, N-N, B-B, Al-Al and C-Al, N-Al and B-Al non.bonded interactions.

Non-bonded interaction	ε_{a-b} (eV)	σ_{a-b}(Å)
C-C [33]	0.00296	3.407
N-N [34]	0.00910	4.289
B-B [35]	0.00412	3.453
Al-Al [36]	0.41570	2.620
C-Al	0.03508	3.014
N-Al	0.06167	3.455
B-Al	0.04136	3.037

avoid strong repulsive interactions at the beginning of the simulation. The Al atoms within this interior rectangular space were removed. The nanofillers were then inserted into the respective Al prisms (oriented with their length direction coinciding with the length orientation of the Al prism), ensuring a distance of 2 Å between the nanofiller atoms and the Al atoms along the nanocomposite interface (see Fig. 2).

2.2. Force fields and MD methodology

The mechanical properties of five nanocomposites were explored by performing MD simulations using the Large-Scale Atomic/Molecular Massively Parallel Simulator (LAMMPS) [26] package. Visualization/analysis of the nanocomposites simulations was done with the aid of Visual Molecular Dynamics (VMD) [27] and Open Visualization tool OVITO [28]. The interatomic interactions between C-C, C-N, and C-B atoms are described by the Tersoff potential [29], using the parameters adjusted by Kinaci et al. [30]. Interactions between Al and Al atoms are modelled using the embedded atom model (EAM) potential. The EAM potential parameters are obtained for the Al-Al interaction from Mendelev et al. [31].

No Al-C, Al-N and Al-B bonds are introduced to model the nanofillers-Al interface. Therefore, only vdW forces describe this interaction. The Lennard-Jones (LJ) 12–6 interaction potential (Eq. (1)) is utilized to model the non-bonded interactions between nanofillers and Al matrix material.

$$E_{LJ} = 4\varepsilon\left[\left(\frac{\sigma}{r}\right)^{12} - \left(\frac{\sigma}{r}\right)^{6}\right] \tag{1}$$

where E_{LJ} is the LJ potential energy, ε is the coefficient of well-depth energy, σ is the vdW equilibrium distance of null potential and r is the distance between atom pairs. The LJ parameters for the interactions between nanofiller atoms (C, N and B) and Al atoms are calculated by the Lorentz-Bertholet mixing rule (Eq. (2) and Eq. (3)) [32]:

$$\varepsilon_{a-b} = \sqrt{\varepsilon_{a-a}\varepsilon_{b-b}} \tag{2}$$

$$\sigma_{a-b} = \frac{1}{2}(\sigma_{a-a} + \sigma_{b-b}) \tag{3}$$

The value of ε_{a-b} was obtained from Eq. (2) between ε_{a-a} (C, N or B) and ε_{b-b} (Al). The value of σ_{a-b} was obtained from Eq. (3) between σ_{a-a} (C, N or B) and σ_{b-b} (Al). Table 2 resumes the LJ well-depth and interatomic distance parameter values for C-C, N-N, B-B and Al-Al non-bonded interactions taken from Refs. [33,34,35,36] and includes the calculated parameters for the C-Al, N-Al and B-Al non-bonded interactions. A cutoff distance of 10.0 Å was chosen for the LJ nanofillers-Al interfacial interactions, which is larger than 2.5 σ_{a-b} [37,38], in order to avoid truncation errors and to fit to the cutoff distance of the Tersoff potential [30,39].

2.3. Melting and recrystallization

Hou et al. [40] investigated the cooling rate dependence of the solidification of liquid Al. The system was heated to 1173 K in a isothermal-isobaric (NPT) ensemble, equilibrated, and then cooled to 273 K at different cooling rates (0.1–10 K/ps). A timestep of 2 fs was used. They concluded that a cooling rate of approximately 1 K/ps is the upper limit to obtain a developed Al crystalline structure. Kumar [41] studied the orientation of Al atoms over the graphene substrate. The author equilibrated the nanocomposite at 2500 K (for melting and to obtain a uniform distribution of Al atom in the liquid state), in an NPT ensemble, and then used a cooling rate of 1 K/ps to cool the nanocomposite from 2500 K to 10 K in 2500 ps. Later, the author and his research group [42], in a similar work, equilibrated two systems (pure Al and Al graphene nanoflakes composites) at 1500 K for 20 ns. Then, decreased the temperature of the systems from 1500 to 300 K at a cooling rate of 0.1 K/ps. A lower cooling rate was adopted to efficiently capture the evolution of various nanocrystalline structures. In these two works, they did not specified timestep. Faria et al. [25] equilibrated pristine Al prism and the nanocomposites at 1500 K and 1 atm for 300 ps, in a NPT ensemble. Then, used a cooling rate of 1 K/ps to cool the systems from 1500 K to 10 K (timestep = 1 fs, 1,490,000 timesteps).

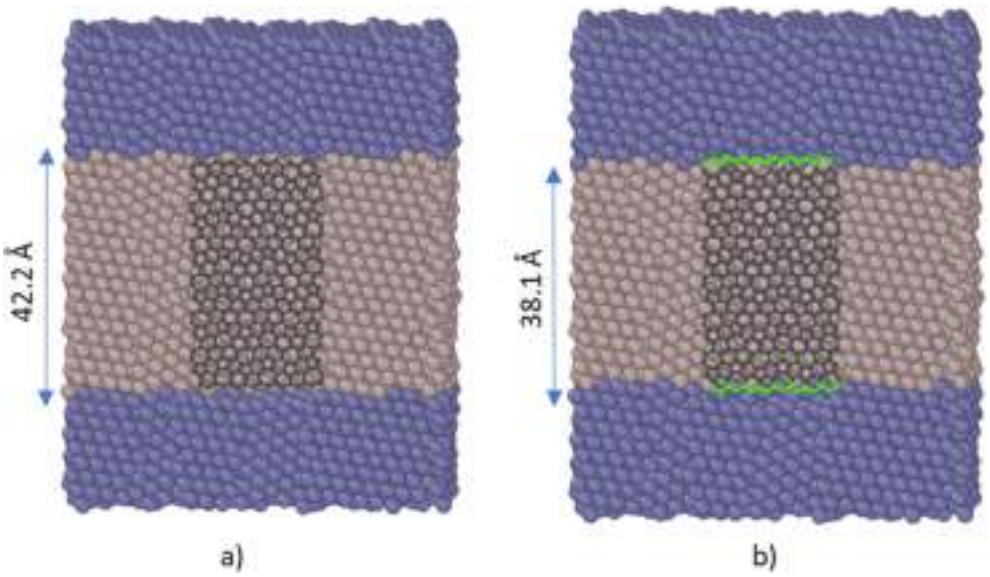

Fig. 3. Representation of the boundary conditions (purple and green atoms) applied to Al-phagraphene nanocomposite after recrystallization: a) Only the purple Al atoms are fixed at the boundaries (Case A); b) All atoms within the boundaries (purple Al and green nanofiller atoms) are fixed (Case B). (For interpretation of the references to colour in this figure legend, the reader is referred to the web version of this article.)

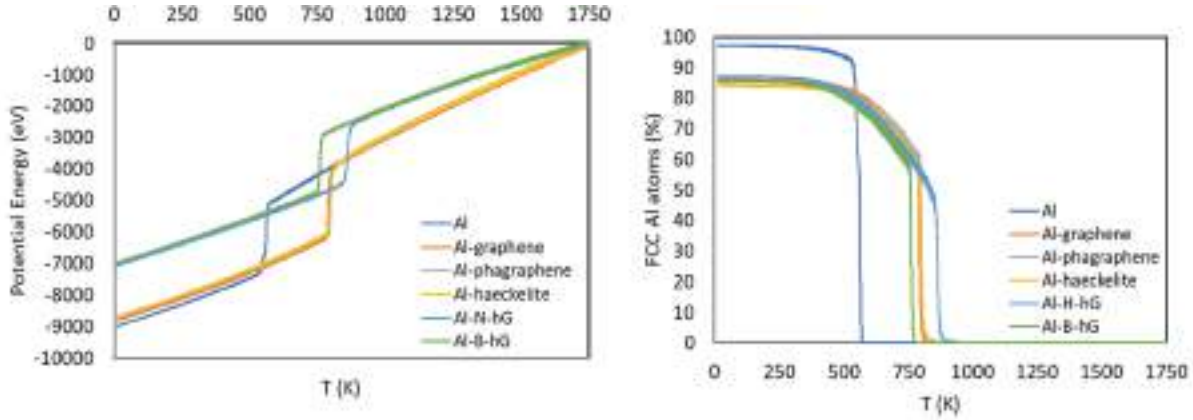

Fig. 4. Temperature dependence of a) potential energy and b) number of Al atoms with FCC crystal structure for pure Al and nanocomposites during recrystallization.

Zhou et al. [43] equilibrated an Al-graphene at 1200 K for 50 ps. Then, they decreased the temperature of system from 1200 K to 300 K at a cooling rate 0.1 K/ps. A timestep of 2 fs was applied, under a NPT ensemble.

In the reported literature [25,40,41,42,43], most of the MD studies used an initial temperature ranging from 1173 to 2500 K and a cooling rate ranging from 0.1 to 10 K/ps for the crystallization process of pure Al or AMCs. In this work, a set of parameters were tested to optimize the recrystallization yields. Based on the literature described and the results obtained (% FCC and mean square displacement MSD), it was found that to obtain a high recrystallization yield, the ideal conditions are i) equilibration at 1750 K and ii) a cooling rate of 0.25 K/ps. Thus, the single-crystal Al prism and the five nanocomposites were equilibrated at 1750 K and 1 atm for 100 ps. After melting, the liquid systems were equilibrated at 1750 K for 500,000 timesteps (timestep = 1 fs), to eliminate abnormal internal residual stresses and to stabilize the nanocomposites. Equilibration was performed within the context of NPT ensemble and the Nosé-Hover thermostat/barostat was used for temperature and pressure control. Then, using a cooling rate of 0.25 K/ps, the systems were cooled from 1750 K to 10 K (timestep = 0.5 fs, 13,920,000 timesteps). After cooling, the solidified systems were also put into a NVT ensemble and equilibrated at 10 K for 500,000 timesteps (timestep = 1 fs). In the melting and cooling process, the nanofillers were kept fixed in the centre of the prism. These two processes were incorporated during the equilibrium stage to achieve a true distribution of the Al atoms in the surface of the nanofillers.

2.4. Tensile loading tests

Recrystallization modified the dimensions of pure Al and its nanocomposites increasing them slightly (see Table A.1 in Annex A). These "new" dimensions were used as initial values of the prisms' volume the calculation of their mechanical properties. After equilibration, tensile loading was applied to pure Al and to the nanocomposites prisms in the [0 0 1] direction. The load imposition method is similar to the one used in previous works [25,44]. Two boundary conditions coincident with the prism bases were defined. Within these two boundaries the atoms are fixed, and their motion is limited to the [0 0 1] direction with an imposed velocity. Tensile loads on the prism are simulated by assigning opposite velocities to these boundary atoms. The described loading method was first employed to the case of pristine Al, which permitted validation of the method by comparing the extracted mechanical

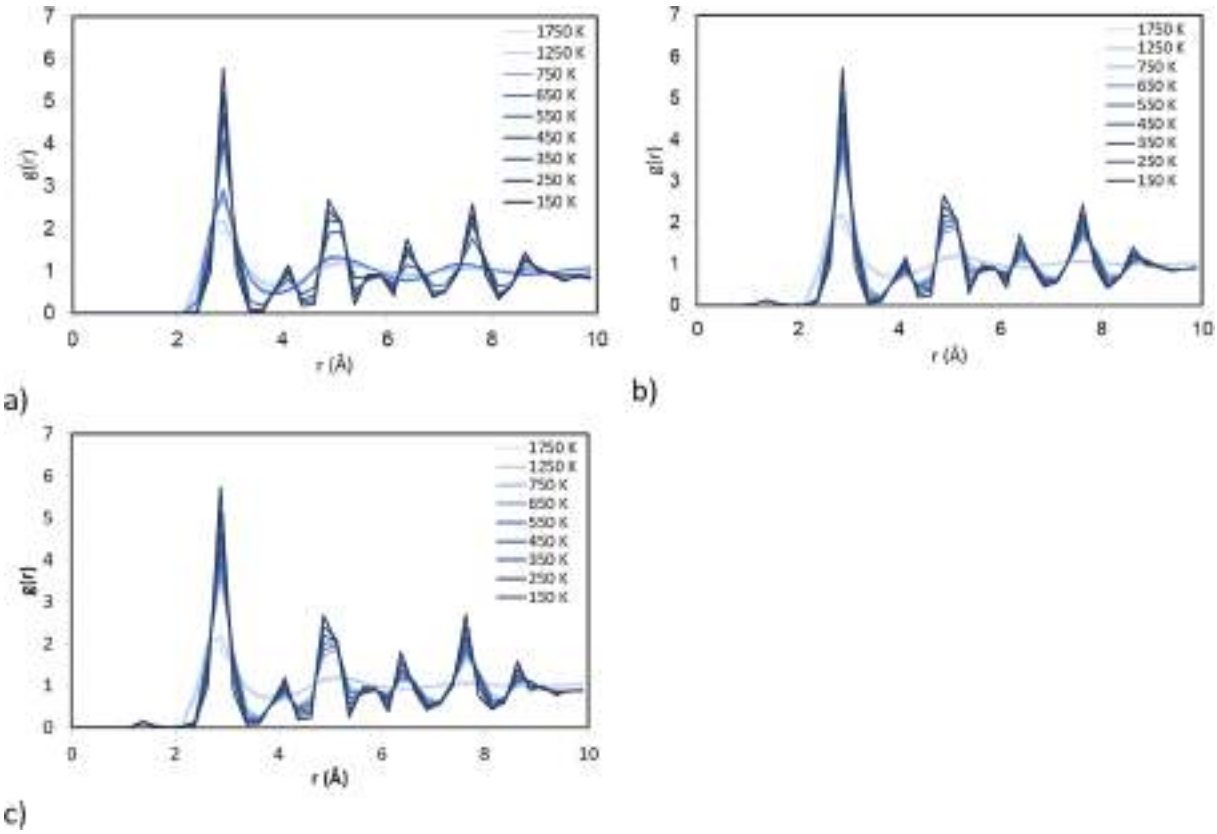

Fig. 5. Radial distribution functions for **a)** pure Al; **b)** Al-graphene; **c)** Al-N-hG at different temperatures.

properties with the ones obtained experimentally [45,46].

In the case of nanocomposites, two different loading conditions were implemented: (i) Case A - only the Al atoms are fixed at the boundaries, i.e., loading is only applied to Al atoms, allowing the nanofillers to move freely within the Al matrix. Only vdW interactions act at the interface; (ii) Case B - all atoms within the boundaries (Al and nanofiller atoms) are fixed, i.e., the nanofiller is bounded within the Al matrix. These two loading conditions correspond to limit situations to what occurs in practice, were the length of the nanofillers, the reactive or non-reactive ends, and the defects define how the ends of the nanofillers can be more or less connected to the Al matrix. A displacement velocity of 0.05 Å/ps was imposed on the fixed atoms of both boundaries, but with opposite directions along the z-axis. In total, Al was stretched by 32.5 Å, eventually leading to rupture before reaching its final length. Young's modulus (Y) was calculated in the elastic range $0 < \varepsilon_z < 0.05$.

The boundary conditions (case A and B) applied to Al-phagraphene can be seen in Fig. 3. A thickness was selected to leave a region of unbound atoms with a length of about 42 Å for case A and 38 Å for case B centered in the prism. It should be noted that the number of nanofiller atoms contained within the two boundaries is equal, but the number of Al atoms fixed per boundary may be slightly different. These two boundary conditions are here considered as limiting cases for flake end-matrix interaction, weak (Case A) or strong (Case B), as such weakening or strengthening of the related composites (accordingly) is expected[1].

[1] In case A, we also provide in appendix B some results of additional simulations conducted by considering an extra layer of Al atoms between the edge of flake and the boundary Al atoms. This was made to verify the sensitivity of the model with respect to the existence of this extra layer of Al atoms.

3. Results and discussion

3.1. Effect of nanofillers in Al recrystallization

The variation of potential energy of Al matrices, with or without nanofillers, during recrystallization is shown in Fig. 4. The potential energy monotonically decreases as the temperature decreases. However, when atoms organize in FCC structures, an abrupt drop in potential energy is observed. This results from the transformation from amorphous state into a more energetically favorable crystalline state which has lower potential energy. When crystal growth ends, the potential energy resumes a linear trend with temperature. From the potential energy profiles, it can be seen that the nucleation temperature for pure Al is about 570 K. Compared to pure Al matrix, the nucleation temperature of the nanocomposites is increased by 300–200 K as a result of the nanofillers reinforcement. Fig. 4b demonstrates the crystal phase growth expressed in number of Al atoms assuming FCC configuration (in percentage) relative to the total number of Al atoms. It confirms that the nucleation temperature for pure Al is around 570 K while for the nanocomposites is around 800–900 K (depending on the nanocomposite). It also shows that the recrystallization yield of pure Al and nanocomposites is always inferior to 100 %. In the case of pure Al, FCC recrystallization yield was 97 %, which indicates that 97 % of Al atoms are aggregated in FCC regions, and only 3 % are solidified in amorphous regions. While in the case of nanocomposites, the relative number of atoms recrystallized in FCC regions, is between 87 and 84 %.

To study the dynamics of the system, MSD of pure Al and nanocomposites during solidification is shown in Fig. C.1a in Appendix C. As temperature decreases, the slope of the MSD curves decreases, which indicates the reduction of moving ranges of the atoms. The temperatures at which the MSD becomes constant coincide with the solidification temperatures for each case, supporting the results obtained in Fig. 4. From the radial distribution function (g(r)) it is also possible to confirm

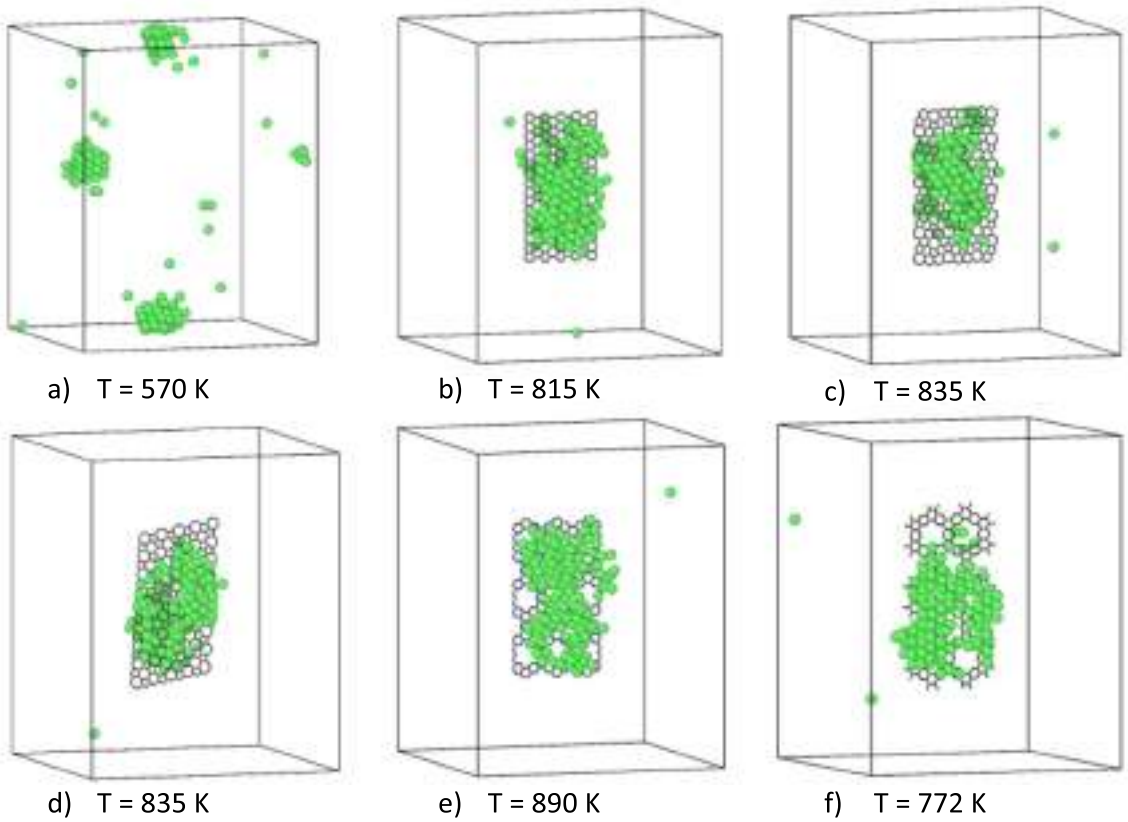

Fig. 6. Snapshots showing the localization of nucleation sites for FCC crystalline clusters on: a) Al; b) Al-graphene; c) Al-phagraphene; d) Al-haeckelite, e) Al-N-hG and **f)** Al-B-hG. Note that Al atoms with FCC structure are colored green, all other atoms are transparent, except C atoms (gray), N atoms (blue) and B atoms (dark green). The respective nucleation temperature is also given. (For interpretation of the references to colour in this figure legend, the reader is referred to the web version of this article.)

the solidification temperatures. The g(r) plot can distinguish amorphous and crystalline phases of Al matrix. In the amorphous phase the distances are uniform, and peaks cannot be distinguished, while in the crystalline phase it is easy to distinguish the peaks, because atoms are at fixed distances. Fig. 5a represents the g(r) of solidification of pure Al for different temperatures. In the amorphous phase, there is a more or less distinct peak at $r = 2.875$ Å. This distance corresponds to the first nearest neighbor of a given Al atom. This value is very near the theoretical value corresponding to $\frac{\sqrt{2}}{2}$•a = 2.863 Å, given that the lattice constant (a) of the FCC structure of Al is 4.05 Å. At r greater than 2.875 Å, distinct and identifiable peaks of g(r) were not found at temperatures above 550 K. This indicates that the Al matrix is in the amorphous phase since only short-range ordered structures are present. For the FCC crystalline state, distinct and multiple peaks of g(r) appeared at $r \geq$ 2.875 Å for the first, second, and next nearest neighbors of the Al atoms with decreasing temperature (below 550 K), due to both short- and long-range ordered structures. Analogous g(r) were calculated for the nanocomposites (see Fig. 5b-c and Fig. C.1 in Appendix C). The g(r) for nanocomposites shows that as the temperature decreases more peaks emerge, and the peaks become higher and sharper, indicating that the Al matrix becomes more ordered at a lower temperature (below 750 K).

The localization of the nucleation sites for Al matrices is shown in Fig. 6 and their growth is presented in Fig. C.2 to Fig. C.7 in Appendix C. The algorithm used to detect crystal structures is the adaptive CNA (Common Neighbor Analysis) algorithm from Stukowski et al. [47] which is based on the original CNA algorithm from Honeycutt et al. [48] but with a variable cutoff. This algorithm is implemented in the OVITO software [28].

In the case of pure Al, nucleation sites occur at multiple sites across the molten matrix. The temperature range where the crystals grow varies from 570 K to 500 K. On the other hand, in the case of nanocomposites, as the temperature decreases, the amorphous Al atoms around nanofillers are the first to be transformed into a well-ordered structure and the nucleation of FCC Al atoms begins in the interface region (see Fig. 6b-f). The organization of atoms in a crystal FCC structure then covers the nanofillers and spreads outwards (see Fig. C.3 to Fig. C.7 in Appendix C). Below 550 K, crystalline FCC structures in nanocomposites are completely formed and encompass 80 % of all the Al atoms in the matrix. These nanofillers promote the nucleation of crystal FCC structures in the nanocomposites, due to their planar surface. They also allow higher nucleation temperatures than those required for pure Al matrix and permit the growth of larger crystal structures practically without grain boundaries. According to Fig. 6b-f, FCC regions began to nucleate on the nanocomposites at: 815 K for Al-graphene; 835 K for Al-phagraphene and Al-haeckelite; 890 K for Al-N-hG; and 772 K for Al-B-hG.

The final structures of the solidified Al matrices are shown in Fig. 7. From Fig. 7a it can be observed that the solidified pure Al matrix is mostly composed of FCC crystallized structures (97 %). The remainder is composed of dispersed, grains of amorphous Al atoms. FCC crystal organization in the nanocomposites is disturbed by stacking faults planes. In fact, FCC crystal organization in Al-graphene is only disturbed by two HCP stacking planes (see Fig. 7b). These planar defects are orientated parallel to the nanofiller plane and are twinning planes, since the delimited FCC crystal regions change orientation. In Al-phagraphene and Al-haeckelite nanocomposites two amorphous stacking planes can be observed (see Fig. 7c-d), however one of the planes corresponds to the

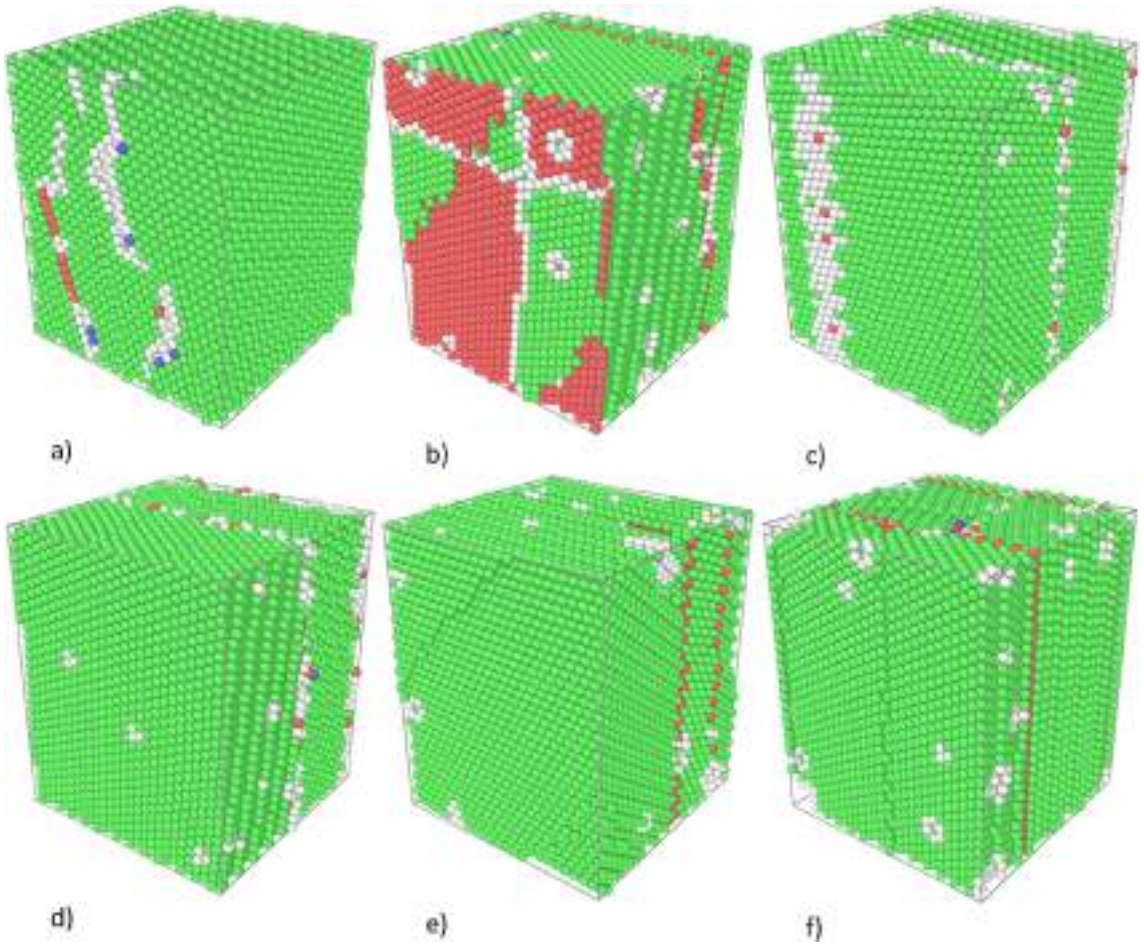

Fig. 7. Structural arrangement, at 10 K (final temperature), of: a) Al; b) Al-graphene; c) Al-phagraphene; d) Al-haeckelite, e) Al-N-hG and **f)** Al-B-hG. Note that Al atoms with FCC structure are colored green, HCP structure are colored red, BCC structure are colored blue and amorphous are colored white. (For interpretation of the references to colour in this figure legend, the reader is referred to the web version of this article.)

interface, which is mainly constituted by amorphous Al atoms. Of the five nanocomposites, these two have the lowest recrystallization yield (84 %). Similarly, to Al-graphene nanocomposite, in Al-N-hG and Al-B-hG nanocomposites FCC crystal organization is comprised of two HCP stacking faults planes parallel to the nanofillers. In the case of Al-B-hG, these planar planes are twinning planes. The recrystallization yields of the Al-N-hG and Al-B-hG nanocomposites are 87 % and 85 %, respectively.

3.2. *Mechanical behaviour of nanocomposites under tensile loading*

The stress–strain responses of pure Al and nanocomposites during tensile deformation are depicted in Fig. 8. Energy-strain curves are described in Fig. C.10 in Appendix C. The mechanical properties of the recrystallized Al and the nanocomposites are presented in Table 3. The nanofillers are fixed and aligned with the loading direction (see Fig. 2 and Fig. 3) before the recrystallization process. The level of recrystallization of pure Al and the nanocomposites, and the elasticity of the nanofillers should be considered in the interpretation of the results. The Young's modulus (Y) of graphene is 813 GPa; the Y of PG is 812 GPa; the Y of haeckelite is 728 GPa; the Y of N-hG is 328 GPa; and the Y of B-hG is 195 GPa. These were calculated using the Tersoff potential [29].

Several differences can be observed in the stress–strain curves (see Fig. 8). These differences are reflected in the mechanical properties obtained for the recrystallized Al and nanocomposites (see Table 3). Overall, when tensile loading is applied only to the Al matrix (case A) in the nanocomposites, their mechanical behavior is identical to that of pure Al. It can also be noted a decrease of both yield stress (σ_y) and yield strain (ε_y) in case A (weak flake end-matrix interaction) for all nanocomposites. On the other hand, when tensile loads are imposed on both matrix and nanofiller (case B, strong weak flake end-matrix interaction), improvements of the mechanical properties of Al are clearly visible.

In stress–strain curves, the elastic zone presents a monotonic slope, while the plastic zone presents a saw-tooth shape, characteristic of metal deformation mechanisms. This effect is more pronounced in matrices with a higher level of crystallization, such as pure Al, Al-graphene, Al-N-hG, and Al-B-hG. The slope of the stress–strain curve of recrystallized Al increases slowly in the elastic zone and exhibits lower stress levels in the plastic zone, than the stress–strain curves of nanocomposites (case B). This behavior, however, is not observed in the Al-N-hG nanocomposite (Fig. 8d), because the sheet in question (N-hG) exhibits high porosity and lower elasticity. Thus, recrystallized Al exhibits values of Y, σ_y and ε_y lower than those of other nanocomposites (except Al-N-hG, see Table 3).

In case B, Al nanocomposites with undoped nanofillers show an increase of Y between 15 % and 27 % (15 % for phagraphene, 16 % for haeckelite and 27 % for graphene) relative to pure Al, while the doped nanofillers do not present a significant increase of Y (see Table 3). These results agree with the fact that the undoped nanofillers have a much higher Y compared to the doped nanofillers (N-hG and B-hG). The size

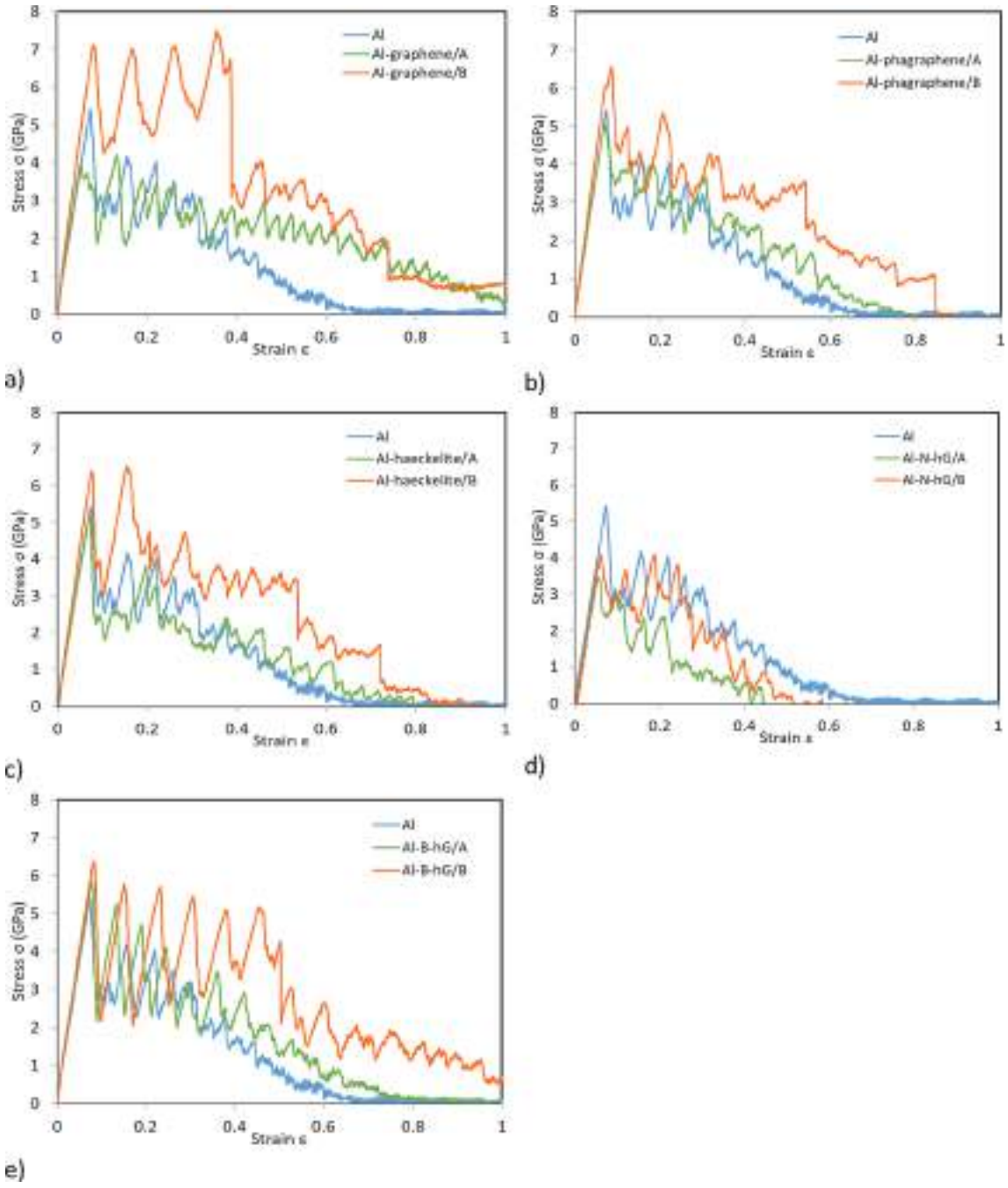

Fig. 8. Stress–strain curves for tensile loading of a) Al-graphene, b) Al-phagraphene, **c)** Al-haeckelite, **d)** Al-N-hG and **e)** Al-B-hG. Cases A (green) and cases B (orange) are compared to pure Al (blue). (For interpretation of the references to colour in this figure legend, the reader is referred to the web version of this article.)

and uniformity of the holes also contributes to these results. The more porous the nanofiller, the lower the reinforcement. This can be proved by comparing the hole size of doped nanofillers with that of undoped nanofillers. The first ones are composed of a periodic array of nanosized holes with larger dimensions (around 6 Å). Focusing on Al nanocomposites with undoped nanofillers, the uniformity of the hole sizes influences the mechanical properties of the nanocomposites, i.e., the more uniform the hole size in the nanofiller, the greater the reinforcement. Graphene being composed solely of rings containing 6 carbon atoms shows more significant improvements in the mechanical properties of the Al matrix than phagraphene or haeckelite which are composed of rings containing 5, 6, 7 carbon atoms. In case A, nanocomposites only suffer very residual distortion in their shape, while in case B, the nanofillers reach fracture generally in their central area. These results can be seen in Fig. C.10 and Fig. C.11 in Appendix C, which depicts the deformed configurations of the studied matrices for the strain of $\varepsilon = 0.20$ and 0.40, respectively.

3.3. *On the application of rule of mixtures for stiffness prediction*

The well-known rules of mixtures, direct and inverse, have been applied to evaluate the stiffness of composite materials. They generally lead to good and fair predictions of the Young's moduli of composite materials. As far as nanomaterials are concerned, they also have been

Table 3
Young's modulus (Y) and Yield stress (σ_y) in GPa, as well as yield strain (ε_y) are presented for pure Al and nanocomposites (Cases A and B). A comparison between the mechanical properties of nanocomposites and pure Al is also given in the form of percentage of variation.

Structure	Y	%	σ_y	%	ε_y	%
Al	76		5.41		0.074	
Al-graphene/A	80	+7	3.93	−27	0.051	−31
Al-graphene/B	95	+27	7.12	+32	0.081	+10
Al-phagraphene/A	75	0	5.05	−7	0.070	−5
Al-phagraphene/B	86	+15	6.54	+21	0.086	+16
Al-haeckelite/A	77	+3	5.21	−4	0.072	−2
Al-haeckelite/B	87	+16	6.40	+18	0.076	+4
Al-N-hG/A	72	−4	3.45	−36	0.055	−25
Al-N-hG/B	75	0	4.08	−25	0.061	−17
Al-B-hG/A	75	0	5.82	+8	0.079	+7
Al-B-hG/B	78	+4	6.37	+18	0.083	+13

investigated but without the same level of success they exhibit at microscale, especially due to quantum effects and complex interatomic forces, which are absent at microscale [49]. The two well-known laws are given by:

$$Y_d = f_f Y_f + \left(1 - f_f\right) Y_m \tag{4}$$

$$Y_i = \left[f_f / Y_f + \left(1 - f_f\right) / Y_m\right]^{-1} \tag{5}$$

where the subscript f denotes the flake (sheet or reinforcement) and m represents the matrix (aluminum), f_f is the fraction of the flake, Y_f and Y_m are the Young's moduli of the flake and matrix, respectively, and Y_d and Y_i denote the Young's modulus of the direct and inverse rule of mixtures, respectively. The direct rule of mixtures simulates the stiffness of two materials (flake and matrix) in parallel, which corresponds precisely to Case B of loading conditions where both materials experience equal strain but different stresses. The inverse rule of mixtures simulates the stiffness of two materials (flake and matrix) in series, which corresponds to Case A of loading conditions where both materials experience equal stress but different strains. In our study, we show two type of fraction f_f: the standard volume fraction of the flake (f_{vol}) and the atomic fraction of the flake (f_{atom}), which is based on the number of atoms. In the latter case, we consider the final dimensions of the nanocomposite RVE after the melting-cooling process (see Table A.1 in Appendix A).

Table 4 shows the main results of this study. It is seen that the volume fraction f_{vol} is lower than the atomic fraction f_{atom} (the ratio f_{vol}/f_{atom}, varying between 1.3 and 2.0) because the volume of an aluminum atom is much higher than the volume of a carbon atom. Expectedly, the Y_{dir} values are always higher than Y_{inv} values. The Y_{inv} values provide a good prediction of the Young's modulus in case A, both for volume fraction and atomic fraction estimates. The difference varies between −4 % and + 6 % in case of volume fraction, while it varies between −4 % and + 7 % in case of atomic fraction. However, the estimation of Y_{dir} using the volume fraction concept provides too low estimates of the Young's modulus in case B, because the difference varies between −14 % and + 4 % with an average of the ratio Y_{dir}/Y_B equal to 0,96. When using the atomic fraction concept, the estimation of Y_{dir} gives more fair values of the Young's modulus in case B. In this case, difference varies between −9 % and + 6 %, and average value of the ratio Y_{dir}/Y_B is 1,00.

4. Conclusion

At an initial stage, the Al matrix and five Al-nanocomposites were melted and recrystallized. Then, tensile loading was applied to the Al matrix and the nanocomposites. Energy-strain and stress–strain curves were obtained and the mechanical properties (elastic modulus, yield strength and yield strain) were determined. The nucleation of FCC crystals in pure Al began at 570 K and the recrystallization yield was about 97 %. The shape and configuration of the nanofillers were found

Table 4
Comparison between the Young's modulus of nanocomposites, computed from MD (Y_A, Y_B) and predicted from direct and inverse rule of mixtures (Y_{inv}, Y_{dir}). The Young's modulus of matrix and flakes, computed from MD, are Y_m = 76 GPa (Aluminium), Y_f = 813 GPa (Graphene), Y_f = 812 GPa (Phagraphene), Y_f = 728 GPa (Haeckelite), Y_f = 328 GPa (N-hG), and Y_f = 195 GPa (B-hG).

Nano Composite	A Y_A (1)	B Y_B (2)	Volume fraction					Atomic fraction				
			f_{vol} (%)	Y_{inv} (3)	Ratio (3)/(1)	Y_{dir} (4)	Ratio (4)/(2)	f_{atom}(%)	Y_{inv} (5)	Ratio (5)/(1)	Y_{dir} (6)	Ratio (6)/(2)
Al-G	80	95	0.71	76.5	0.96	81.2	0.86	1.46	77.0	0.96	86.7	0.91
Al-phaG	75	86	0.80	76.6	1.02	81.9	0.95	1.66	77.2	1.03	88.2	1.03
Al-haeckelite	77	87	0.84	76.6	0.99	81.5	0.94	1.58	77.1	1.00	86.3	0.99
Al-N-hG	72	75	0.91	76.5	1.06	78.3	1.04	1.40	76.8	1.07	79.5	1.06
Al-B-hG	75	78	0.96	76.4	1.02	77.1	0.99	1.26	76.6	1.02	77.5	0.99
				Avg	1.01	Avg	0.96		Avg	1.02	Avg	1.00

to be a crucial factor in the nucleation and growth of FCC crystalline regions. The nucleation temperature of nanocomposites is increased by 300–200 K due to the reinforcement of the nanofillers and, the Al crystallization in nanocomposites was almost complete (between 87 and 84 %). As the temperature decreases, it was found that the amorphous Al atoms around nanofillers are the first to be transformed into a well-ordered structure. Thus, nucleation of FCC Al atoms begins at the interface region. Then covers the nanofillers and spreads outwards.

The mechanical properties of the nanocomposites depend on: (i) the level of crystallization achieved in each matrix; (ii) the interfacial adhesion between the nanofillers and the Al matrix; (iii) the elasticity, porosity and doping of the nanofillers. Al-graphene, Al-phagraphene and Al-haeckelite nanocomposites showed an increase in of Young's modulus, in the case of strong flake end-matrix interaction, between 15 and 27 % relative to pure Al, while Al-N-hG and Al-b-hG do not present such a significant increase. These results agreed with the fact that the undoped nanofillers have a much higher Young's modulus and lower porosity compared to the doped nanofillers (N-hG and B-hG). The application of the rule of mixtures to extract the Young's moduli of the nanocomposite was successful. The inverse rule of mixtures provided good prediction of the Young's modulus in boundary case A, both for volume fraction and atomic fraction estimates. The direct rule of mixtures using the atomic fraction concept provided good predictions of Young's modulus in boundary case B, unlike the volume fraction concept which led to low estimates. In summary, the nanocomposites exhibit higher nucleation temperatures, lower recrystallization yields, and higher mechanical properties (except Al-N-hG and Al-B-hG) when compared to pure Al and in the case of strong flake end-matrix interaction.

The authors declare that they have no known competing financial interests or personal relationships that could have appeared to influence the work reported in this paper.

CRediT authorship contribution statement

Cátia Guarda: Data curation, Formal analysis, Investigation, Methodology, Software, Visualization, Writing – original draft. **Bruno Faria:** Conceptualization, Data curation, Formal analysis, Investigation, Methodology, Software, Visualization, Writing – original draft. **Nuno Silvestre:** Conceptualization, Methodology, Funding acquisition, Supervision, Validation, Writing – review & editing. **José N.C. Lopes:** Conceptualization, Methodology, Funding acquisition, Supervision, Validation, Writing – review & editing. **Nicola M. Pugno:** Validation, Writing – review & editing.

Declaration of Competing Interest

The authors declare that they have no known competing financial interests or personal relationships that could have appeared to influence the work reported in this paper.

Acknowledgements

The first author gratefully acknowledges the financial support given by FCT in the context of the PhD scholarship SFRH/BD/129589/2017. This work was supported by FCT, through IDMEC, under LAETA, project UIDB/50022/2020. This work was supported by FCT, through Centro de Química Estrutural (CQE), project UIDB/00100/2020. The fifth author has received funding from the European Union's Horizon 2020 Research and Innovation Programme under grant agreement GrapheneCore3 no. 881603.

Appendix A

See Table A.1.

Table A1
Values of the dimensions for pure Al and nanocomposites after the cooling process.

Metal/Nanocomposite	H (Å)	%	W (Å)	%	L (Å)	%
Al	66.5	2.6	66.6	2.8	83.0	2.5
Al-graphene	67.0	3.4	65.6	1.2	83.9	3.6
Al-phagraphene	66.6	2.8	66.6	2.8	82.9	2.3
Al-haeckelite	66.6	2.8	65.3	0.8	82.3	1.6
Al-N-hG	67.1	3.5	66.1	2.0	83.5	3.1
Al-B-hG	67.2	3.7	65.7	1.4	83.5	3.1

Appendix B

This appendix provides results of additional simulations by considering an extra layer of Al atoms between the edge of flake and the boundary Al atoms. Table B.1 shows the values of Young's modulus of several nanocompsoites. Expectedly, the value for pure aluminium remained the same. For the cases with aluminium reinforced with flakes (graphene, phagraphene, haeckelite, N-hG, B-hG) the values generally decreased marginally 2–3 %. This is because the addition of extra Al atoms to zones closer to the supported boundaries, which are not strengthened by the flakes, will very slightly decrease the overall stiffness of the composite. However, this drop is marginal because the stiffness of those parts is much lower (some orders of magnitude) than the central part, which is reinforced by the flake.Fig. B1.

Table B1
Values of Young's modulus (GPa) in boundary case A, considering an extra layer of Al atoms between the edge of flake and the boundary Al atoms.

Nano Composite	**No layer** – Fig. 3	**With layer** – Fig. B.1
Al	76	76
Al-graphene	80	78
Al-phagraphene	75	73
Al-haeckelite	77	77
Al-N-hG	72	70
Al-B-hG	75	74

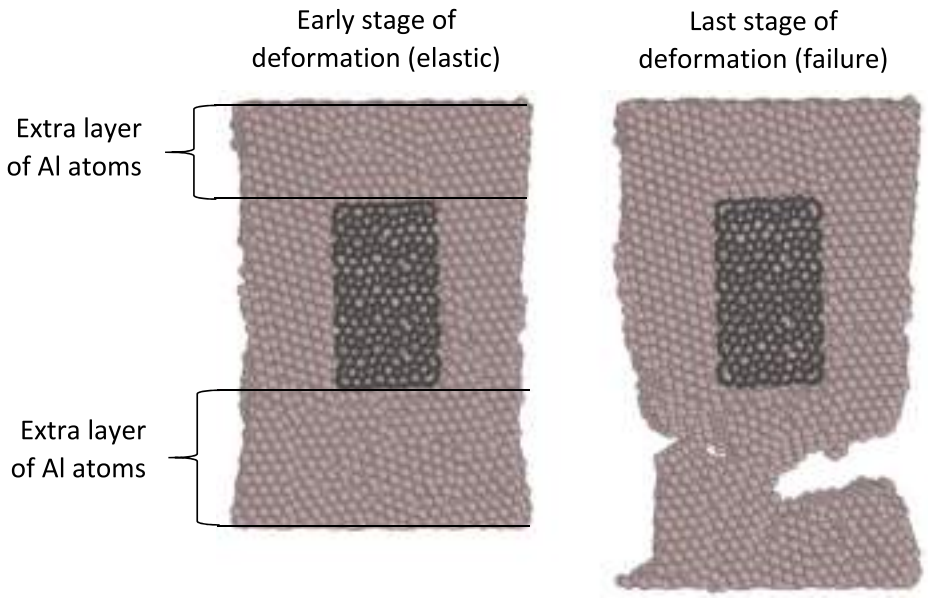

Fig. B1. Deformed shapes of the nanocomposite in boundary case A, in two different stages of deformation: elastic and failure (the Al boundary atoms are not shown here for simplification).

Appendix C

Figs. C1-C11.

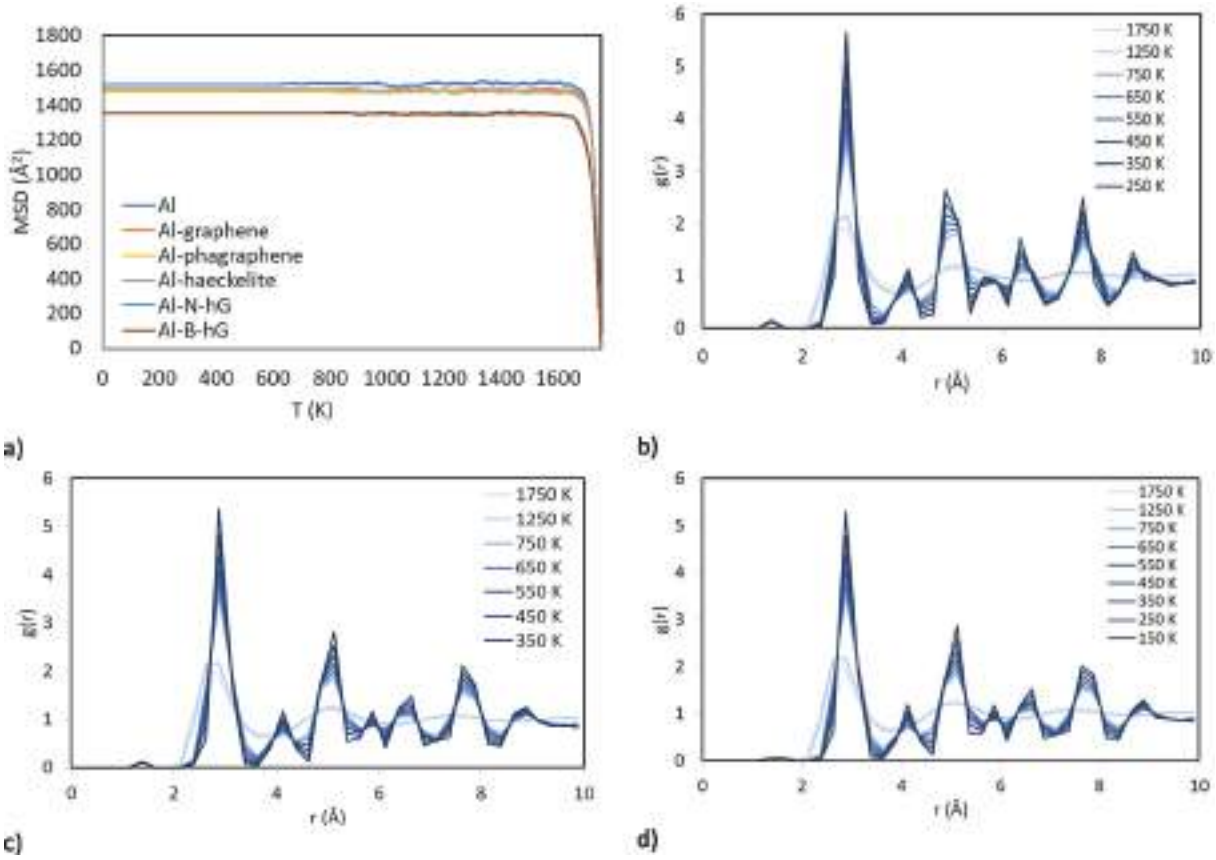

Fig. C1. a) Mean square displacement (with temperature for pure Al and nanocomposites. Radial distribution functions, $g(r)$, at decreasing temperatures (from 1750 K to 150 K) for the recrystallization process of b) Al-phagraphene; c) Al-haeckelite; d) Al-B-hG nanocomposites.

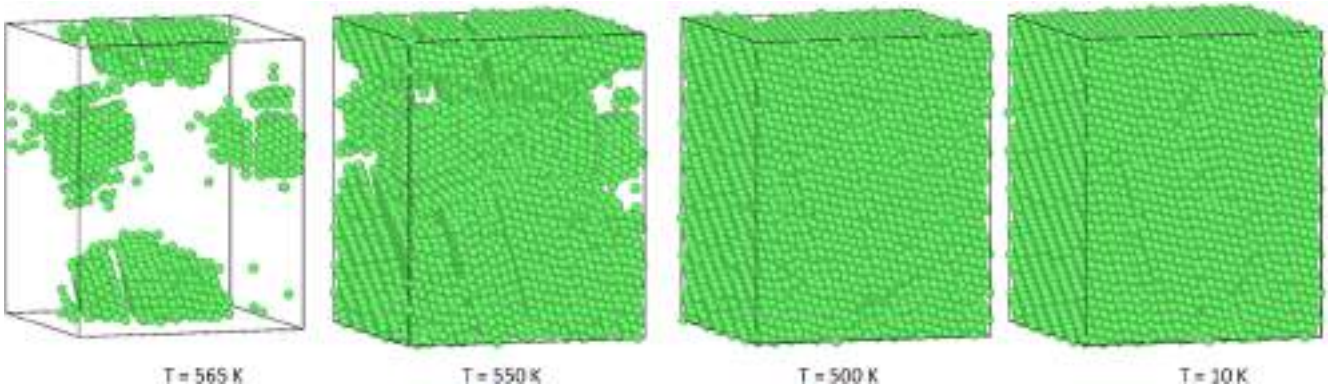

Fig. C2. Snapshots showing the growth and merging of FCC crystalline clusters with decreasing temperature for pure Al. Note that Al atoms with FCC structure are colored green, all other atoms are transparent. The respective nucleation temperature is also given. (For interpretation of the references to colour in this figure legend, the reader is referred to the web version of this article.)

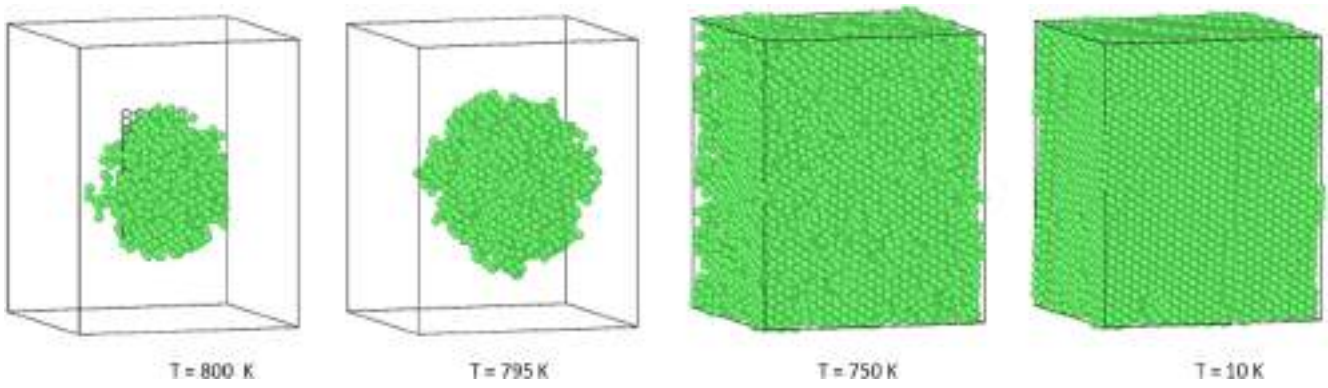

Fig. C3. Snapshots showing the growth and merging of FCC crystalline clusters with decreasing temperature for Al-graphene. Note that Al atoms with FCC structure are colored green, all other atoms are transparent, except C atoms (gray). The respective nucleation temperature is also given. (For interpretation of the references to colour in this figure legend, the reader is referred to the web version of this article.)

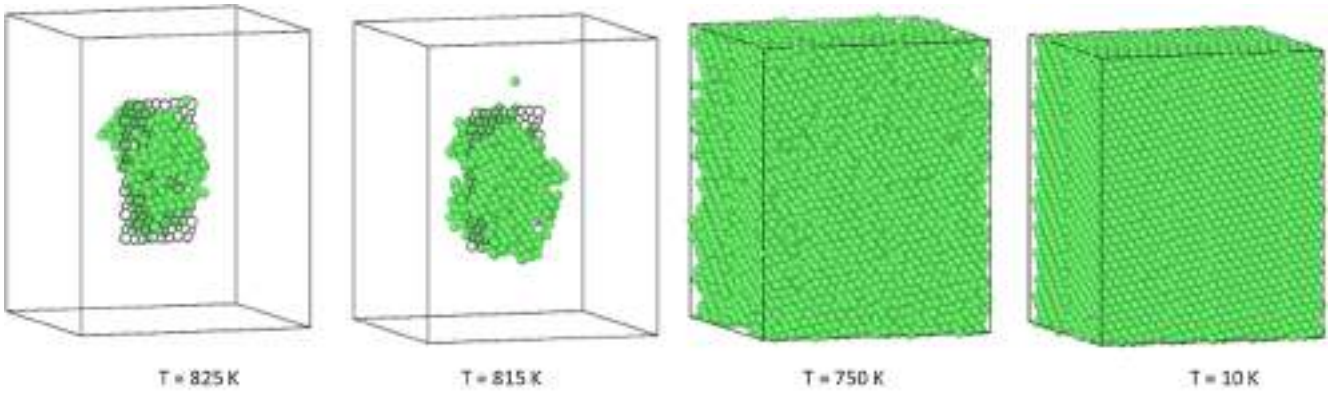

Fig. C4. Snapshots showing the growth and merging of FCC crystalline clusters with decreasing temperature for Al-phagraphene. Note that Al atoms with FCC structure are colored green, all other atoms are transparent, except C atoms (gray). The respective nucleation temperature is also given. (For interpretation of the references to colour in this figure legend, the reader is referred to the web version of this article.)

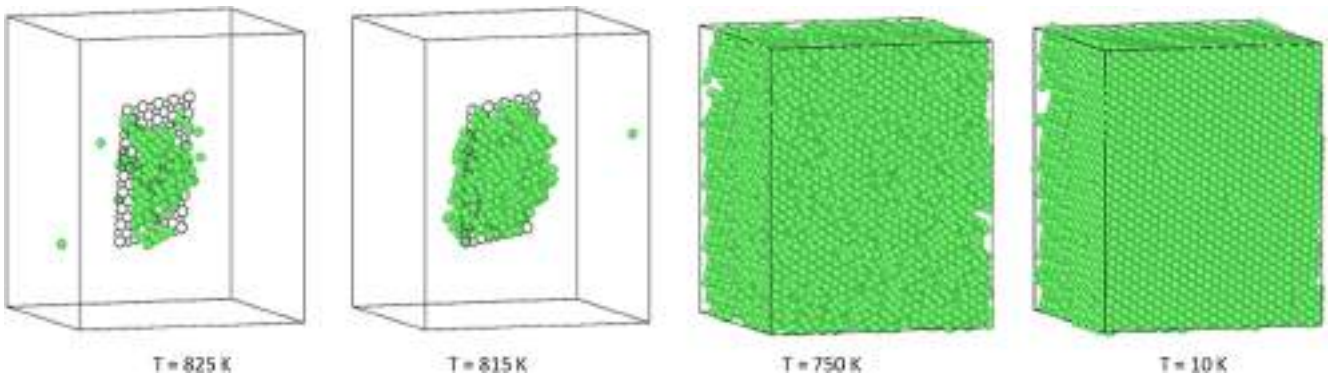

Fig. C5. Snapshots showing the growth and merging of FCC crystalline clusters with decreasing temperature for Al-haeckelite. Note that Al atoms with FCC structure are colored green, all other atoms are transparent, except C atoms (gray). The respective nucleation temperature is also given. (For interpretation of the references to colour in this figure legend, the reader is referred to the web version of this article.)

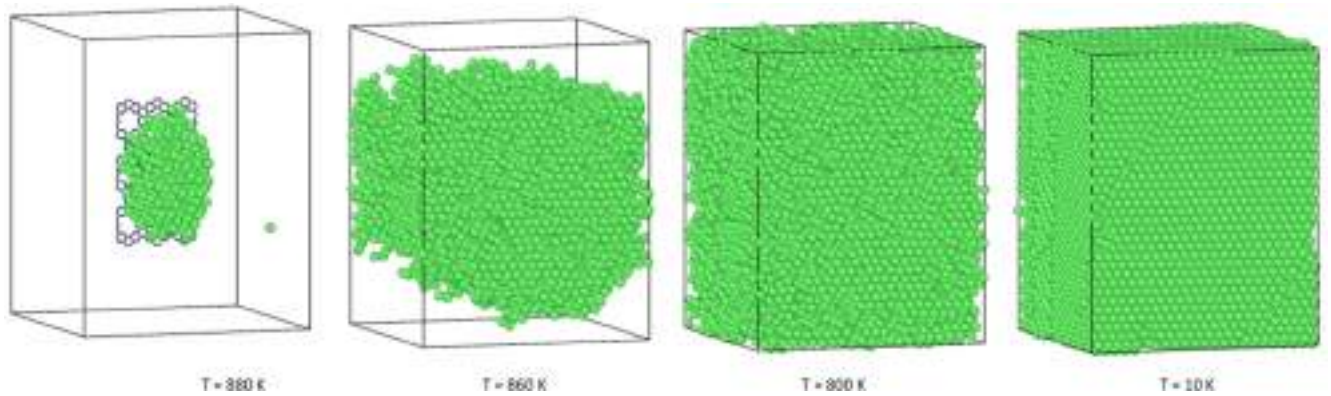

Fig. C6. Snapshots showing the growth and merging of FCC crystalline clusters with decreasing temperature for Al-N-hG. Note that Al atoms with FCC structure are colored green, all other atoms are transparent, except C atoms (gray) and N atoms (blue). The respective nucleation temperature is also given. (For interpretation of the references to colour in this figure legend, the reader is referred to the web version of this article.)

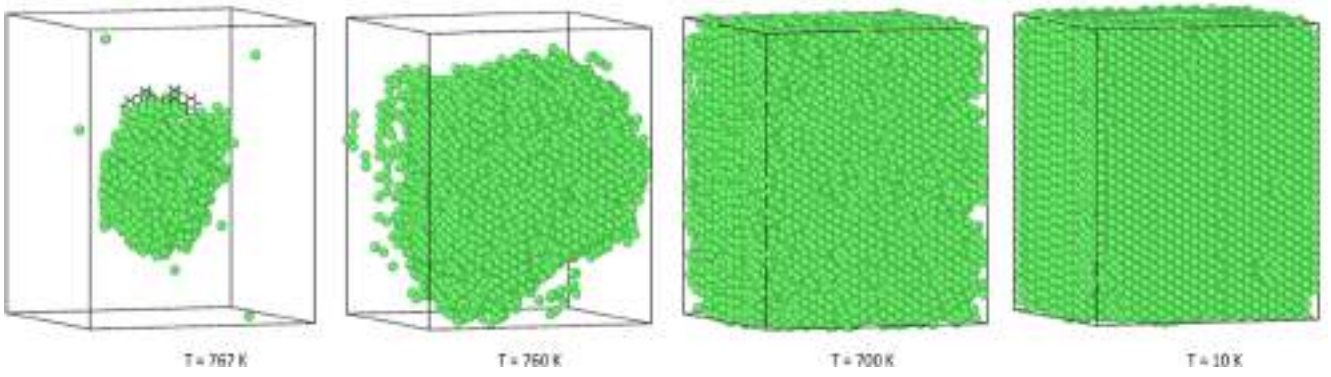

Fig. C7. Snapshots showing the growth and merging of FCC crystalline clusters with decreasing temperature for Al-B-hG. Note that Al atoms with FCC structure are colored green, all other atoms are transparent, except C atoms (gray) and B atoms (dark green). The respective nucleation temperature is also given. (For interpretation of the references to colour in this figure legend, the reader is referred to the web version of this article.)

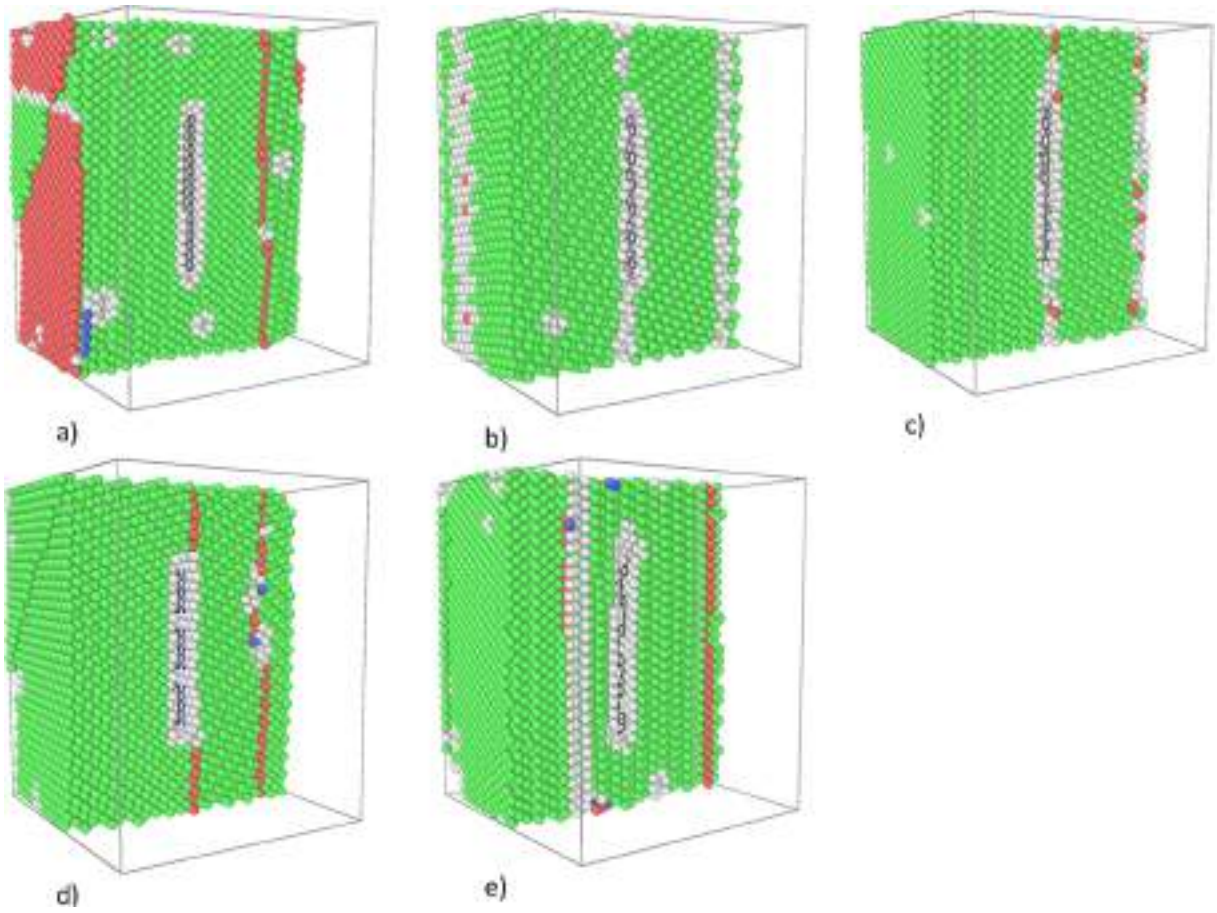

Fig. C8. Structural arrangement, at 10 K (final temperature), of: a) Al-graphene; b) Al-phagraphene; c) Al-haeckelite, d) Al-N-hG and f) Al-B-hG. Note that Al atoms with FCC structure are colored green, HCP structure are colored red, BCC structure are colored blue and amorphous are colored white. (For interpretation of the references to colour in this figure legend, the reader is referred to the web version of this article.)

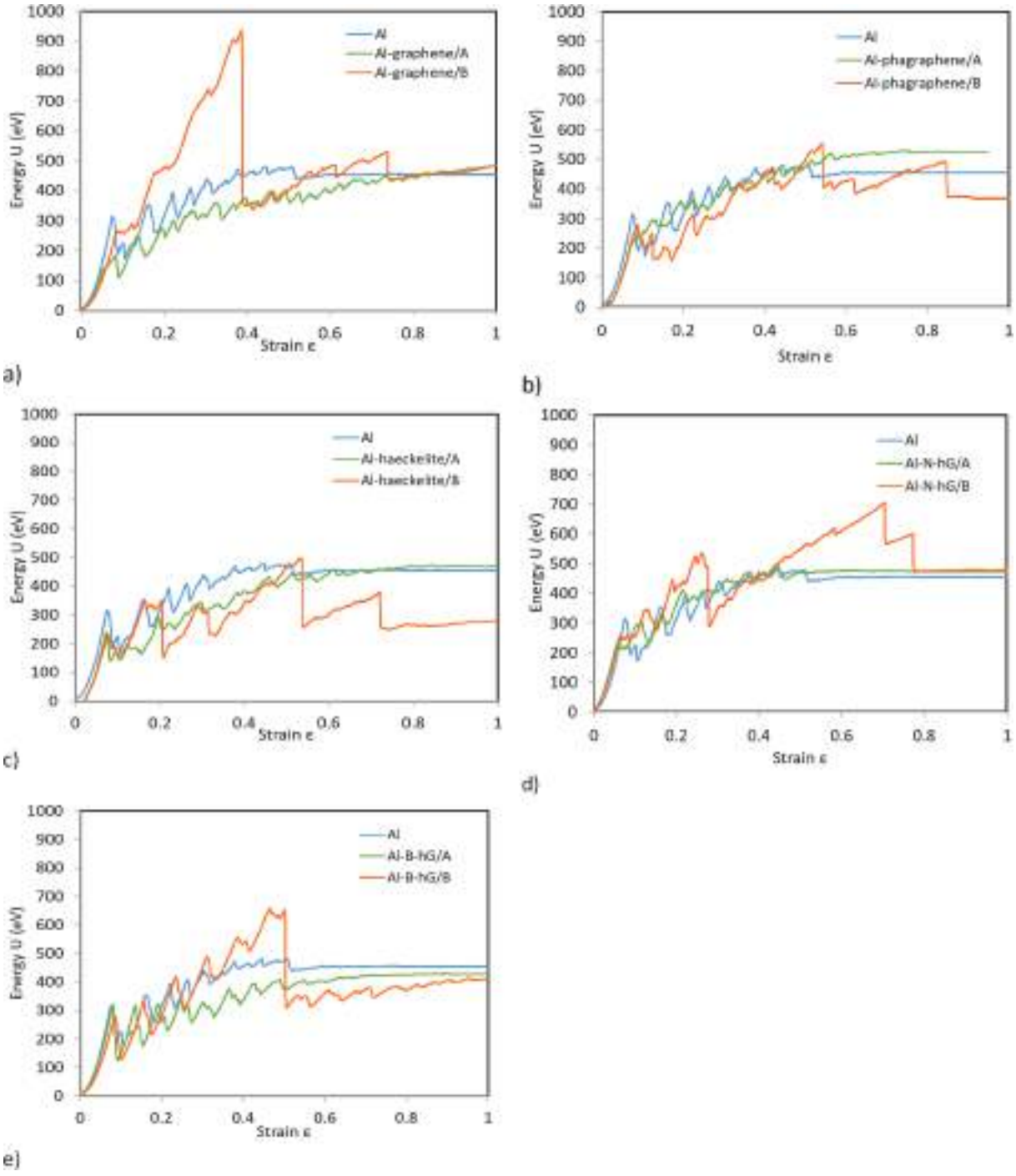

Fig. C9. Energy-strain curves for tensile loading of a) Al-graphene, b) Al-phagraphene, **c)** Al-haeckelite, **d)** Al-N-hG and **e)** Al-B-hG. Cases A (green) and cases B (orange) are compared to pure Al (blue). (For interpretation of the references to colour in this figure legend, the reader is referred to the web version of this article.)

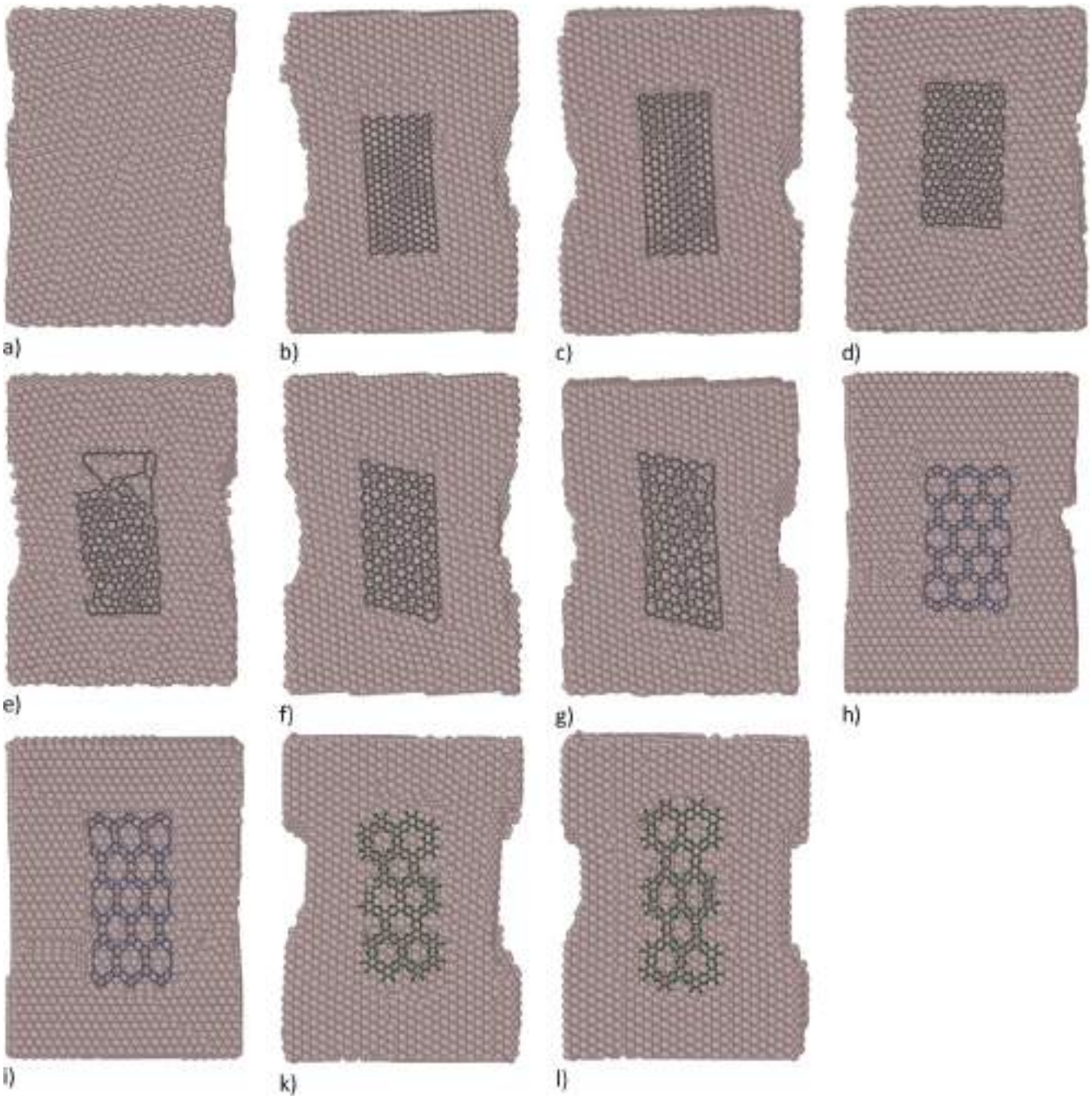

Fig. C10. Deformed configurations of Al and nanocomposites for 20% strain ($\varepsilon = 0.2$): **a)** Al; **b)** Al-graphene/A; **c)** Al-graphene/B; **d)** Al-haeckelite/A; **e)** Al-haeckelite/B; **f)** Al-phagraphene/A; **g)** Al-phagraphene/B; **h)** Al-N-hG/A; i) Al-N-hG/B; **k)** Al-BN-hG/A and **l)** Al-B-hG/B.

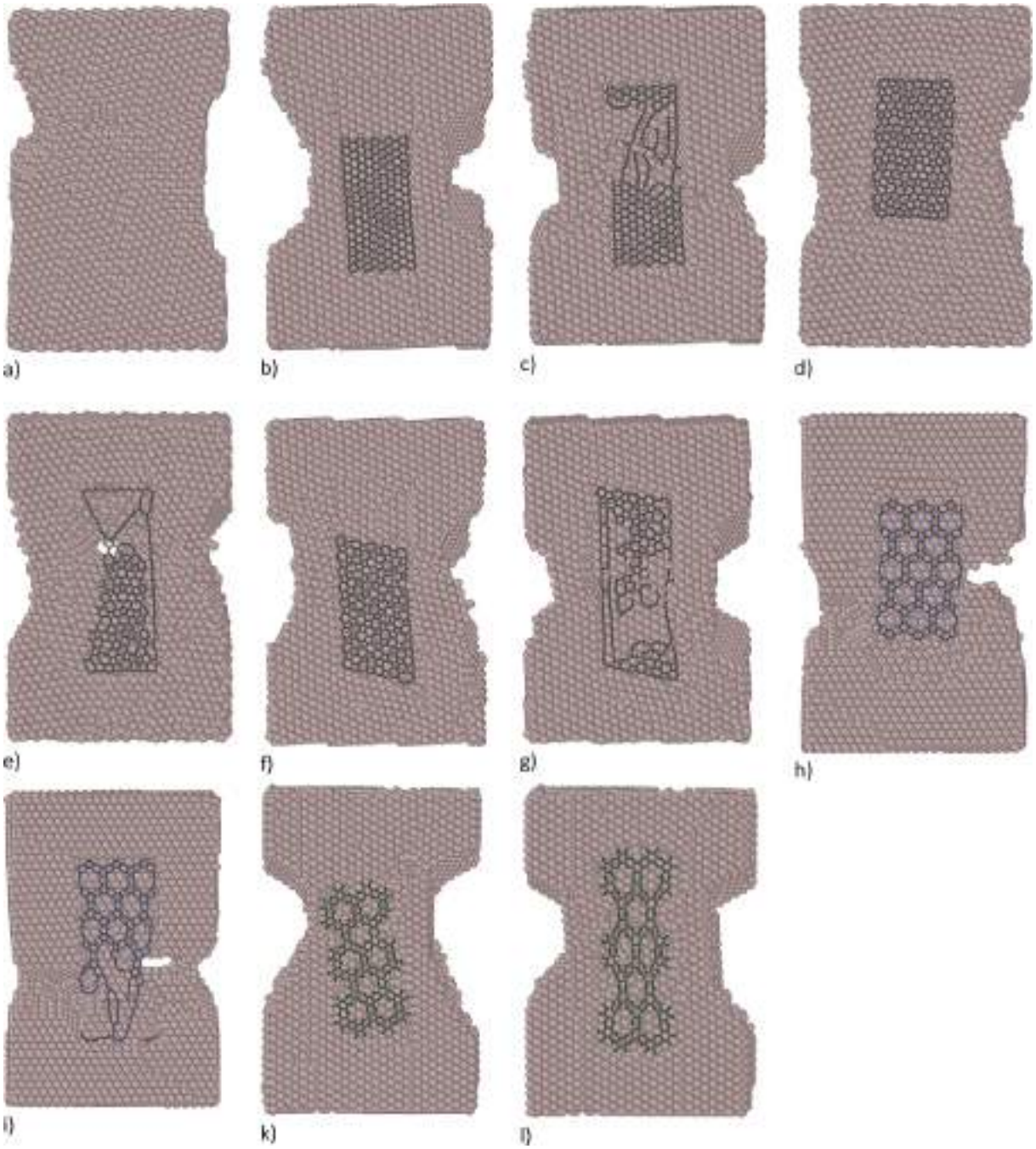

Fig. C11. Deformed configurations of Al and nanocomposites for 40% strain ($\varepsilon = 0.4$): **a)** Al; **b)** Al-graphene/A; **c)** Al-graphene/B; **d)** Al-haeckelite/A; **e)** Al-haeckelite/B; **f)** Al-phagraphene/A; **g)** Al-phagraphene/B; **h)** Al-N-hG/A; **i)** Al-N-hG/B; **k)** Al-BN-hG/A and **l)** Al-B-hG/B.

References

[1] Su J, Teng J. Recent progress in graphene-reinforced aluminum matrix composites. Frontiers of Materials Science 2021;15(1):79–97.
[2] Zhang X, Wang S. Interfacial Strengthening of Graphene/Aluminum Composites through Point Defects: A First-Principles Study. Nanomaterials 2021;11(3):738. https://doi.org/10.3390/nano11030738.
[3] Memarian F, Fereidoon A, Darvish Ganji M. Graphene Young's modulus: Molecular mechanics and DFT treatments. Superlattices Microstruct 2015;85:348–56.
[4] Shao T, et al. Temperature dependent elastic constants and ultimate strength of graphene and graphyne. J Chem Phys 2012;137:194901.
[5] Zhu Y, et al. Graphene and Graphene Oxide: Synthesis, Properties, and Applications. Adv Mater 2010;22:3906–24.
[6] Wang J, Li Z, Fan G, Pan H, Chen Z, Zhang Di. Reinforcement with graphene nanosheets in aluminum matrix composites. Scr Mater 2012;66(8):594–7.
[7] Güler O, Bağcı N. A short review on mechanical properties of graphene reinforced metal matrix composites. J Mater Res Technol 2020;9:6806–33.
[8] Ghazaly A, Seif B, Salem HG. Mechanical and Tribological Properties of AA2124-Graphene Self Lubricating Nanocomposite. Light Metals 2013:411–5.
[9] Pradhan SK, et al. Graphene-incorporated aluminum with enhanced thermal and mechanical properties for solar heat collectors. AIP Adv 2020;10:065016.
[10] Meng J, et al. Microstructure and wear resistance of graphene-reinforced aluminum matrix composites. Mater Res Express 2019;6:026517.
[11] Li Z, Fu X, Guo Q, Zhao L, Fan G, Li Z, et al. Graphene quality dominated interface deformation behavior of graphene-metal composite: The defective is better. Int J Plast 2018;111:253–65.
[12] Moon J, Yang S, Cho M. Interfacial strengthening between graphene and polymer through Stone-Thrower-Wales defects: Ab initio and molecular dynamics simulations. Carbon 2017;118:66–77.
[13] Chu Ke, Wang J, Liu Y-P, Geng Z-R. Graphene defect engineering for optimizing the interface and mechanical properties of graphene/copper composites. Carbon 2018;140:112–23.
[14] Du X, Du W, Wang Z, Liu Ke, Li S. Defects in graphene nanoplatelets and their interface behavior to reinforce magnesium alloys. Appl Surf Sci 2019;484:414–23.
[15] Li D, Song S, Zuo D, Wu W. Effect of Pore Defects on Mechanical Properties of Graphene Reinforced Aluminum Nanocomposites. Metals 2020;10(4):468. https://doi.org/10.3390/met10040468.
[16] Lokhande AC, Qattan IA, Lokhande CD, Patole SP. Holey graphene: an emerging versatile material. J Mater Chem A 2020;8(3):918–77.
[17] Yang T, et al. Tailoring pores in graphene-based materials: from generation to applications. J Mater Chem A 2017;5:16537–58.
[18] Wang Z, et al. Phagraphene: A Low-Energy Graphene Allotrope Composed of 5–6–7 Carbon Rings with Distorted Dirac Cones. Nano Letter 2015;15:6182–6.
[19] Terrones H, Terrones M, Hernández E, Grobert N, Charlier J-C, Ajayan PM. New Metallic Allotropes of Planar and Tubular Carbon. Phys Rev Lett 2000;84(8):1716–9.
[20] Mortazavi B, Rahaman O, Rabczuk T, Pereira LFC. Thermal conductivity and mechanical properties of nitrogenated holey graphene. Carbon 2016;106:1–8.
[21] Nafday D, et al. Boronated holey graphene: a case of 2D ferromagnetic metal. PCCP 2019;21:21128–35.
[22] Pereira LFC, et al. Anisotropic thermal conductivity and mechanical properties of phagraphene: a molecular dynamics study. RSC Adv 2016;6:57773.
[23] Openov LA, Podlivaev AI. Thermal stability of diamond-like carbon nanothreads. JETP Lett 2016;104(3):193–6.
[24] Sui C, et al. Morphology-Controlled Tensile Mechanical Characteristics in Graphene Allotropes. ACS Omega 2017;2:3977–88.
[25] Faria B, Guarda C, Silvestre N, Lopes JNC. Aluminum composites reinforced by γ-graphynes: The effect of nanofillers porosity and shape on crystal growth and composite strengthening. Comput Mater Sci 2020;176:109538.
[26] Plimpton S. Fast Parallel Algorithms for Short-Range Molecular Dynamics. J Comput Phys 1995;117(1):1–19.
[27] Humphrey W, Dalke A, Schulten K. VMD: Visual molecular dynamics. J Mol Graph 1996;14(1):33–8.
[28] Stukowski A. Visualization and analysis of atomistic simulation data with OVITO-the Open Visualization Tool. Modell Simul Mater Sci Eng 2010;18:015012.
[29] Tersoff J. Modeling solid-state chemistry: Interatomic potentials for multicomponent systems. Physical Review B 1989;39(8):5566–8.
[30] Kinaci A, et al. Thermal conductivity of BN-C nanostructures. Physical Review B 2012;86:115410.
[31] Mendelev MI, et al. Analysis of semi-empirical interatomic potentials appropriate for simulation of crystalline and liquid Al and Cu. Phil Mag 2008;88:1723–50.
[32] Boda D, Henderson D. The effects of deviations from Lorentz-Berthelot rules on the properties of a simple mixture. Molecular Physics: An International Journal at the Interface Between Chemistry and Physics 2008;106:2367–70.
[33] Kutana A, Giapis KP. Transient deformation regime in bending of single-walled carbon nanotubes. Phys Rev Lett 2006;97:245501.
[34] Vekeman J, et al. Nitrogen Gas on Graphene: Pairwise Interaction Potentials. International Conference on Computational Science and Its Applications 2018;10964:563–78.
[35] Fan L, Yao W. Mechanical properties of a G/h-BN heterobilayer nanosheets coupled by interlayer sp3 defects. Mater Res Express 2019;6:095075.
[36] Munilla J, Castro M, Carnicero A. Surface effects in atomistic mechanical simulations of Al nanocrystals. Physical Review B 2009;80:024109.
[37] Khurana L, Srivastava AK, Dikshit MK, Pathak VK. A Molecular Dynamics Study of the Buckling Behaviour of Graphene-Reinforced Aluminum Nanocomposite Plate. Materials Physics and Mechanics 2019;42:234–41.
[38] Zhang S, Huang P, Wang F. Graphene-boundary strengthening mechanism in Cu/graphene nanocomposites: A molecular dynamics simulation. Mater Des 2020;190:108555.
[39] Choi BK, Yoon GH, Lee S. Molecular dynamics studies of CNT-reinforced aluminum compositesunder uniaxial tensile loading. Compos B 2016;91:119–25.
[40] Hou ZY, et al. Cooling rate dependence of solidification for liquid aluminium: a large-scale molecular dynamics simulation study. PCCP 2016;18:17461–9.
[41] Kumar S. Graphene engendered aluminium crystal growth and mechanical properties of its composite: an atomistic investigation. Mater Chem Phys 2018;208:41–8.
[42] Kumar S, Pattanayek SK, Das SK. Reactivity-Controlled Aggregation of Graphene Nanoflakes in Aluminum Matrix: Atomistic Molecular Dynamics Simulation. The Journal of Physical Chemistry C 2019;123:18017–27.
[43] Zhou X, et al. Atomic simulations of the formation of twist grain boundary and mechanical properties of graphene/aluminum nanolaminated composites. Comput Mater Sci 2020;172:109342.
[44] Faria B, et al. CNT-reinforced iron and titanium nanocomposites: Strength and deformation mechanisms. Compos B Eng 2020;187:107836.
[45] Haque MA, A Saif MT. Mechanical behavior of 30–50 nm thick aluminum films under uniaxial tension. Scr Mater 2002;47(12):863–7.
[46] Daghfas O, Znaidi A, Ben Mohamed A, Nasri R. Experimental and numerical study on mechanical properties of aluminum alloy under uniaxial tensile test. Fattura ed Integrità Strutturale 2017;11(39):263–73.
[47] Stukowski A. Structure identification methods for atomistic simulations of crystalline materials. Modell Simul Mater Sci Eng 2012;20:045021.
[48] Honeycutt JD, Andersen HC. Molecular dynamics study of melting and freezing of small Lennard-Jones clusters. The Journal of Physical Chemistry 1987;91:4950–14932.
[49] Hernandez Y, Nicolosi V, Lotya M, Blighe FM, Sun Z, De S, et al. High-yield production of graphene by liquid-phase exfoliation of graphite. Nat Nanotechnol 2008;3(9):563–8.